# Quantitative Electromagnetic Inversion of Irregular Scatterers Based on a Threefold Hybrid Method

Yanjin Chen, Li-Ye Xiao, *Member, IEEE*, Jianliang Zhuo, Feng Han, *Senior Member, IEEE*, and Qing Huo Liu, *Fellow, IEEE*

***Abstract*— This article presents a threefold hybrid electromagnetic inversion method that combines the linear sampling method (LSM), the convolutional neural network (CNN), and the full-wave inversion (FWI). The whole inversion procedure includes three steps. First, the LSM qualitatively reconstructs the preliminary shapes and locations of the scatterers. Then, the CNN U-Net is used to further refine the shapes of the scatterers. At last, the Born iterative method (BIM) is implemented to quantitatively invert for the permittivity and conductivity of inhomogeneous scatterers or multiple homogeneous scatterers inside the downsized inversion domain. Numerical experiments show that compared with the pure FWI method BIM, the proposed hybrid method can achieve both higher reconstruction accuracy and lower computational cost. Besides this superiority, the proposed hybrid method also has strong adaptability to multiple scatterers with high contrasts even when the measured field data are contaminated by large noise. Laboratory experimental data are also used to verify the feasibility of the proposed method.**

***Index Terms*— Convolutional neural network (CNN), electromagnetic (EM) inversion, full-wave inversion (FWI), linear sampling method (LSM).**

## I. Introduction

ELECTROMAGNETIC (EM) inversion is to infer the model parameters such as shapes, locations, or constitutive parameters of the scatterers placed inside the domain of interest (DOI) from the scattered field measured at the receiver arrays outside the DOI. It has wide applications for geophysical exploration [1], medical imaging and diagnosis [2], radar remote sensing [3], security screening [4], through-wall imaging [5], etc.

According to the requirements of application scenarios, EM inversion can be divided into two categories: qualitative inversion and quantitative inversion. Qualitative inversion, also known as imaging, can obtain the approximate shapes and locations of unknown targets at a relatively low cost. The common qualitative inversion methods include the reverse time migration (RTM), Kirchhoff migration, linear sampling method (LSM), and factorization method (FM). RTM migration and Kirchhoff migration are widely employed in subsurface detection [6], [7] by the ground-penetrating radar (GPR). RTM is based on the extrapolation of full-wave fields and thus has higher imaging accuracy for complex subsurface structures than Kirchhoff migration. In addition, it adapts to steeper dips in subsurface structures. By contrast, Kirchhoff migration computes the traveling time based on ray tracing. It has lower computational cost than RTM but also sacrifices imaging accuracy. The principle of LSM is completely different from that of the migration method. In the LSM, no broadband wavefield extrapolation is needed. Instead, the multistatic far-fields measured at a fixed frequency when the incident fields are from several directions are supposed to be radiated by a focusing point source in the inversion domain [8], [9]. FM is similar to LSM but provides a mathematically rigorous and exact characterization of the scatterers and thus also requires structural assumptions for the scatterers that are not required by LSM [10]. The advantage of these qualitative inversion methods is their low computational cost. However, they can rarely reconstruct the constitutive parameters of the unknown scatterers. Another drawback is that the obtained shapes are always distorted when the scatterers have irregular geometry, e.g., nonconvex envelopes or sharp corners.

The quantitative inversion is able to reconstruct both the shapes and dielectric parameters of irregular scatterers. At present, the most frequently used quantitative method is the full-wave inversion (FWI). A rigorous cost function is constructed and the model parameters including the permittivity, conductivity, positions, shapes, or others of the scatterers are simultaneously solved. The major mathematical techniques to solve the cost function include the Newton-type method and gradient descent method. The Newton method has the merit of fast convergence which is widely adopted in the geophysical exploration by EM waves [11]. However, the computation of the Hessian matrix is unaffordable in the 3-D voxel-based inversion. Therefore, the inexact Newton method is proposed to strike a compromise between the speed and accuracy [12]. Compared with the Newton-type method, the gradient descent method has a lower cost of a single iteration step for an EM inverse scattering problem. For example, the Born iterative method (BIM) [13] starts from Born approximation and solves the discretized data equation

Manuscript received September 13, 2020; revised March 25, 2021; accepted May 11, 2021. Date of publication June 2, 2021; date of current version December 16, 2021. This work was supported by the National Key Research and Development Program of the Ministry of Science and Technology of China under Grant 2018YFF01013300. *(Corresponding author: Feng Han.)*

Yanjin Chen, Li-Ye Xiao, Jianliang Zhuo, and Feng Han are with the Key Laboratory of Electromagnetic Wave Science and Detection Technology, Institute of Electromagnetics and Acoustics, Xiamen University, Xiamen 361005, China (e-mail: feng.han@xmu.edu.cn).

Qing Huo Liu is with the Department of Electrical and Computer Engineering, Duke University, Durham, NC 27708 USA (e-mail: qhliu@duke.edu).

Color versions of one or more figures in this article are available at https://doi.org/10.1109/TAP.2021.3083775.

Digital Object Identifier 10.1109/TAP.2021.3083775

using the conjugate gradient method [14]. Different from BIM, contrast source inversion (CSI) has no forward computation. The induced current and dielectric contrasts in the inversion domain are updated alternately until the total mismatches reach minima [15]. The subspace optimization method (SOM) is similar to CSI but the induced current is decomposed into two parts, the deterministic part and the ambiguous part [16]. Although the quantitative inversion can simultaneously retrieve the geometry and dielectric parameters of unknown scatterers, iteration is inevitable due to the intrinsic nonlinearity of the data equation. Consequently, the computational cost also increases.

In recent years, machine learning, especially deep learning (DL), quickly attracts the attention of EM inversion researchers since it can circumvent the traditional time-consuming iterations and retrieve model parameters of the scatterers almost in a real-time fashion. The DL methods for EM inversion can roughly be categorized into four kinds [17]. The first kind is the direct learning approach in which the artificial neural network (ANN) is treated as a black box and the model parameters of the scatterers are directly reconstructed from the scattered fields by the ANN. The direct inversion scheme proposed in [18], the complex-valued deep convolutional neural network (CNN) in [19], and the nonlinear mapping module in [20] can be classified as the direct learning approach. The second kind is the learning-assisted objective-function approach in which the inverse problems are still solved by minimizing the cost function. However, some components of the iterative solver are learned, which expedites the iterations. For example, in [21] and [22], the supervised descent method is first employed to learn the Jacobian matrix in offline training. In the online prediction, the model parameters are reconstructed in a short period of time. Another type of learning-assisted inversion is to use the CNN to obtain preliminary dielectric images of scatterers. Then, iterations of FWI are implemented starting from these preliminary images. For example, in [23], [24], the trained CNN can predict dielectric images from magnetic resonance or ultrasound images of tissues, and then the iterative solver will refine the dielectric parameter distribution of the tissues. In [25], the Contrast Source Net is proposed to learn the total contrast source, which effectively improves the reconstruction accuracy of the iterative solver. The third kind is the physics-assisted learning approach in which the domain knowledge is incorporated into the input or the internal architecture of ANNs. The backpropagation scheme in [18], the DeepNIS in [26], and the combination of Born approximation and U-Net in [27] can be classified as physics-assisted learning. Usually, a linear approximation inverse solver provides the preliminary profiles (including the dielectric parameter values) of the scatterers which are input into the ANNs. Besides these three kinds, there are also other ways to apply machine learning to EM inversion. For example, in [28], the induced current learning method is designed to incorporate physics into the ANNs. In [29], the unsupervised machine learning 3-D Markov random field model is used to classify the discretized cells of the inversion domain. Summary and review of the machine learning applications to EM inversion can be referred to [17], [30].

In this article, we propose a threefold hybrid EM inversion scheme, which combines the LSM, BIM, and the ANN. First, LSM is used to quickly determine the approximate locations and shapes of scatterers to compress the inversion domain of FWI. Then, the CNN U-Net is employed to obtain accurate locations and shapes of scatterers. At last, the iterative solver BIM is employed to quantitatively reconstruct the dielectric parameters of scatterers. Due to the compressed inversion domain located by LSM, the ill-posedness in the FWI is alleviated and the computational cost is reduced. However, the images of the scatterers from LSM are not precise enough, especially when there are multiple scatterers with high contrasts. So, we insert the CNN U-Net between LSM and BIM solvers to improve the scatterer images from LSM. In other words, U-Net is used to find the precise compressed inversion domain which coincides with the scatterer shape. This work is different from the learning-assisted objective-function approaches in [21], [22], and [25] since no component of the BIM solver is learned by the CNN. Instead, the CNN is independent of the BIM solver and only helps to reduce the inversion domain size for BIM. It is also different from the learning-assisted imaging methods presented in [23] and [24] and the physics-assisted learning approaches in [18], [26], and [27] since the CNN U-Net is only used to classify the LSM images in the way of pixel by pixel, and the dielectric parameters of scatterers are completely obtained by BIM. In addition, one should note that although the direct learning approaches in [18]–[20] can quantitatively reconstruct the dielectric profiles of the scatterers in a real-time fashion and the design of the ANN is also straightforward, it must spend the unnecessary cost to train and learn underlying wave physics of EM scattering. The last work worth mentioning is [31] in which the qualitative inversion method RTM is used to find the approximate inversion domain before the implementation of FWI. However, in this work, the inversion domain further collapses into the scatterers themselves with the aid of U-Net.

The organization of this article is given as follows. In Section II, the LSM, the forward model, and the inversion model for FWI and the U-Net are described in detail. In Section III, three numerical examples are used to verify the proposed method. In Section IV, the laboratory experimental data are used to validate the hybrid method. Finally, in Section V, the conclusion and future work are presented.

## II. Methods

In this section, first, the formulas of LSM are briefly introduced. Then the full-wave forward and inverse scattering formulas are concisely described in the framework of integral equations. Finally, the configuration of the CNN U-Net is given in detail.

### A. LSM

As shown in Fig. 1, $\Omega$ denotes the DOI, $\Sigma \subseteq \Omega$ is the support of the scatterers, and transmitters and receivers lie on a cycle $\Gamma$ located in the far-zone (i.e., at a distance $R > 10\lambda$, where $\lambda$ is the wavelength). Therefore, the incident

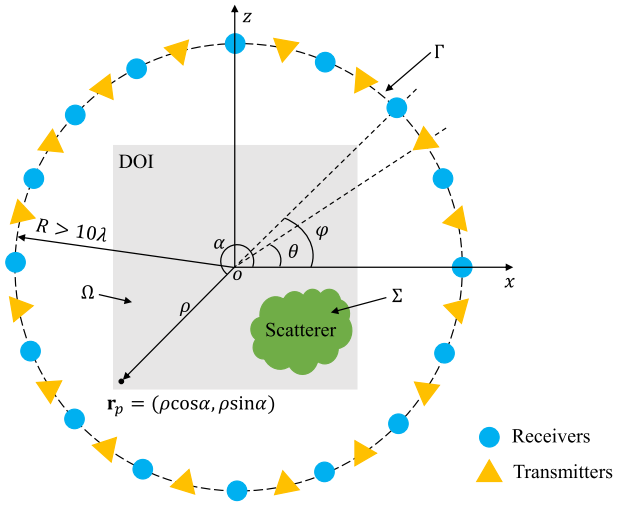


Fig. 1. 2-D imaging and FWI model configuration.

and scattered EM fields can be approximately treated as plane waves. Suppose there are totally $N_t$ transmitters and $N_r$ receivers. $E_y^{sct}(\theta, \varphi)$ is the scattered electric field measured by the receiver in the direction $\varphi$, when the EM wave is radiated by the transmitter in the direction $\theta$, as shown in Fig. 1. For a generic point $\mathbf{r}_p = \hat{x}\rho\cos\alpha + \hat{z}\rho\sin\alpha \in \Omega$, the purpose of LSM is to solve the "far-field" integral equation [8], [9]

$$\int_\Gamma E_y^{sct}(\theta, \varphi) g(\theta, \mathbf{r}_p) d\theta = \sqrt{\frac{2}{\pi k R}} \exp\left[j\frac{\pi}{4} + jk\rho\cos(\varphi - \alpha)\right] \tag{1}$$

in the unknown $g(\theta, \mathbf{r}_p)$, where $k$ is the wavenumber in the background medium. The right-hand side of (1) is the large-argument asymptotic form of the 2-D Green's function, i.e., the Hankel function. It represents the far-field radiated on $\Gamma$ by a 2-D elementary source located in the generic point $\mathbf{r}_p$. We can see that LSM actually is to cast the measured EM fields on $\Gamma$ into the far-field cylindrical symmetrical waves radiated by the focusing point source $\mathbf{r}_p$ in the support $\Sigma$ of the scatterer. The amplitude $|g(\mathbf{r}_p)|$ approaches infinite large when $\mathbf{r}_p$ does not belong to the support $\Sigma$ of scatterers [8], [9]. Therefore, it is always used as an indicator of $\Sigma$.

We then discretize the DOI $\Omega$ into several independent pixels. For $\mathbf{r}_p$ belonging to an arbitrary pixel and the combination of all transmitters and receivers, (1) can be rewritten in the matrix form

$$\mathbf{Fg} = \mathbf{f}(\mathbf{r}_p) \tag{2}$$

where $\mathbf{F}$ is a matrix with the dimension of $N_r \times N_t$ and includes scattered fields measured at the receiver array for different transmitters. $\mathbf{g}$ is a vector having the dimension of $N_t$ and $\mathbf{f}$ is a vector with the dimension of $N_r$. The regularized solution of (2) can be obtained

$$\hat{\mathbf{g}} = \arg\min_{\mathbf{g}} \|\mathbf{Fg} - \mathbf{f}\|_2^2 + \gamma \|\mathbf{g}\|_2^2 \tag{3}$$

where $\|\|_2$ denotes the $L_2$ norm and $\gamma$ is the Tikhonov regularization factor, which avoids the existence of nonradiating sources and prevents sources from having the infinite energy [9], [32]. The closed-form solution of (3) is

$$\hat{\mathbf{g}} = (\mathbf{F}^\dagger\mathbf{F} + \gamma\,\mathbf{I})^{-1}\mathbf{F}^\dagger\mathbf{f} \tag{4}$$

where $\dagger$ denotes the matrix hermitian. For $\mathbf{r}_p$ in a certain pixel, it is likely belonging to the background if $\|\hat{\mathbf{g}}\|_2$ is large. Otherwise, it is judged to belong to the scatterers.

### B. Full-Wave Forward and Inversion Models

The full-wave forward and inverse scattering models are also shown in Fig. 1. The state equation used to formulate the forward scattering is expressed as

$$E_y^{inc}(\boldsymbol{\rho}) = E_y^{tot} + \frac{jk_0^2}{4}\int_\Omega \chi_\epsilon(\boldsymbol{\rho}') E_y^{tot}(\boldsymbol{\rho}') H_0^{(2)}(k_0|\boldsymbol{\rho} - \boldsymbol{\rho}'|) d\boldsymbol{\rho}' \tag{5}$$

where $E_y^{inc}$ is the incident electric field in $\Omega$ and $E_y^{tot}$ is the total electric field in $\Omega$. $k_0$ is the wavenumber in free space and $H_0^{(2)}$ is the 0th-order Hankel function of the second kind. The contrast $\chi_\epsilon$ is expressed as

$$\chi_\epsilon(\boldsymbol{\rho}) = \epsilon_r(\boldsymbol{\rho}) - 1 \tag{6}$$

where $\epsilon_r = \varepsilon_r + (\sigma/j\omega)$ is complex relative permittivity. Equation (5) can be discretized and solved by the stabilized biconjugate-gradient fast Fourier transform (BCGS-FFT) method. The details can be found in [33] and will not be repeated here.

The inverse scattering is formulated by the data equation that can be expressed as

$$E_y^{sct}(\boldsymbol{\rho}) = -\frac{jk_0^2}{4}\int_\Omega \chi_\epsilon(\boldsymbol{\rho}') E_y^{tot}(\boldsymbol{\rho}') H_0^{(2)}(k_0|\boldsymbol{\rho} - \boldsymbol{\rho}'|) d\boldsymbol{\rho}'. \tag{7}$$

In the iterative inversion computation, (7) is discretized, and the contrast $\chi_\epsilon$ is solved by BIM with the total variational (TV) regularization. The cost function in the $(k+1)$th iteration is constructed as

$$\mathbf{C}_{k+1} = \frac{\|\mathbf{s} - \mathbf{A}\mathbf{y}_{k+1}\|_2^2}{\|\mathbf{s}\|_2^2} + \eta\frac{\left\|\sqrt{(\mathbf{D}_x\mathbf{y}_{k+1})^2 + (\mathbf{D}_z\mathbf{y}_{k+1})^2}\right\|_1}{\left\|\sqrt{(\mathbf{D}_x\mathbf{y}_k)^2 + (\mathbf{D}_z\mathbf{y}_k)^2}\right\|_1} \tag{8}$$

where the vector $\mathbf{s}$ contains the measured scattered fields at the receiver array, the vector $\mathbf{y}$ is composed of the contrasts of all the unknown dielectric parameters for all the discretized pixels in the inversion domain, $\mathbf{A}$ is the Fréchet derivative matrix, $\eta$ is the regularization factor, $\mathbf{D}_x$ and $\mathbf{D}_z$ are the discrete difference matrices in $\hat{x}$ and $\hat{z}$ directions, respectively, [34], and $\|\cdot\|_1$ denotes the $L_1$-norm. In the conventional FWI, (5) and (7) are solved alternately by BCGS-FFT-BIM, and thus, the total fields and contrasts are updated alternately until the data misfit reaches a stop criterion. In addition, one should note that the square root in (8) acts on the sum of squares in the way of pixel by pixel. The cost function is minimized by converting the TV regularization term to $L_2$ regularization term, which is called the iteratively reweighted norm algorithm and details can be found in [34].

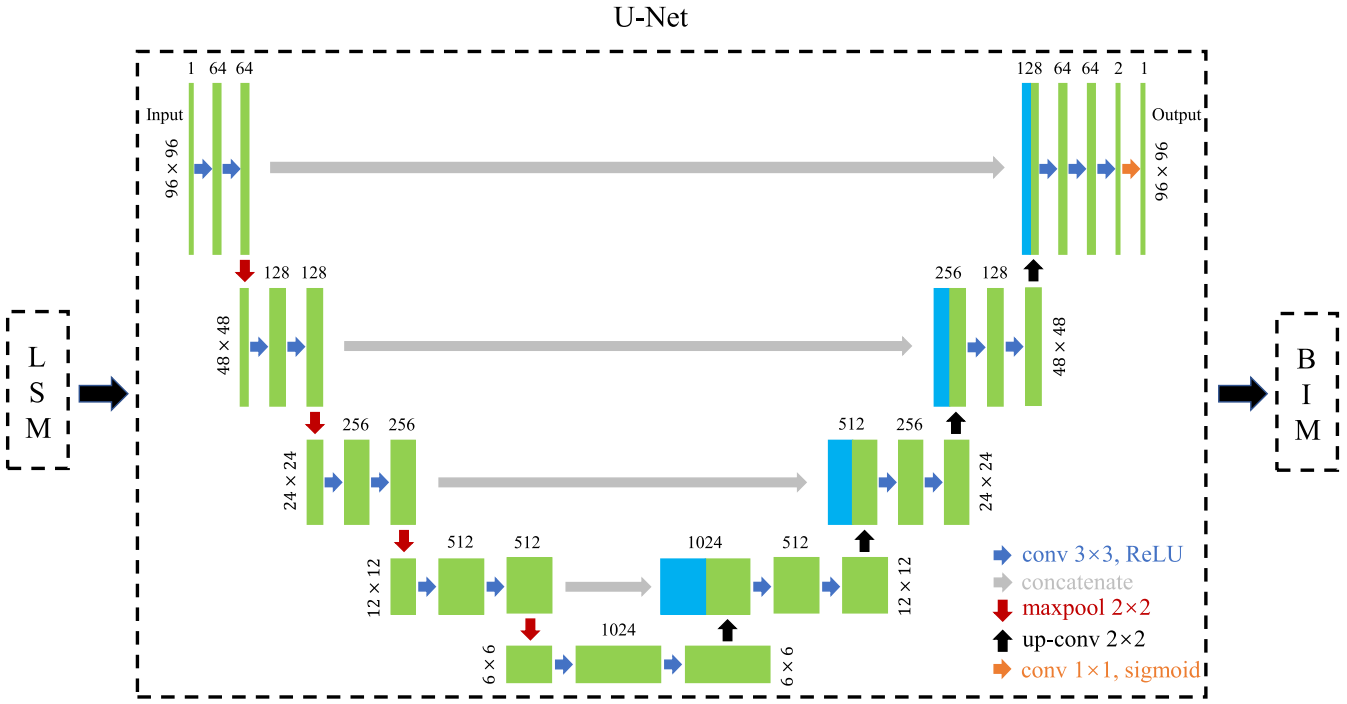


Fig. 2. Architecture of the threefold hybrid inversion scheme. It includes three parts: the LSM, the U-Net, and the BIM.

### C. CNN U-Net

In this article, we choose U-Net to classify LSM results at the pixel level, which was originally proposed for biomedical image segmentation [35]. The architecture of U-Net used in this article is shown in the dotted box of Fig. 2. It is divided into two parts, the encoder (left side) and decoder (right side). The encoder is used for feature extraction and includes four same modules. Each module has two $3 \times 3$ convolution layers with the ReLu activation function and a $2 \times 2$ max-pooling layer. After each downsampling, the number of channels is doubled and the size is reduced by half. The decoder restores the high-level semantic feature map obtained by the encoder to the resolution of the original image and gives it to the classifier for the pixel-level classification. The decoder also contains four same modules. Each module has a $2 \times 2$ upsampling convolution layer with the ReLu activation function and two $3 \times 3$ convolution layers also with the ReLu activation function. The classifier at the last layer of the network is a $1 \times 1$ convolution layer with the sigmoid activation function. Skip-connection between the encoder and decoder layers concatenates the high-level features and low-level features. The high-level features have low resolution and contain more semantic information and are helpful for classifying. The low-level features have high resolution and contain more structural information and are helpful for accurate segmentation. Therefore, skip-connection plays a supplementary role to remedy the information loss of down sampling. Because there are only two classes, "scatterer" and "background," we input the result of LSM and get a binary image displaying the category of each pixel.

We choose the dice loss as the cost function for training. It is based on the dice coefficient which is used to measure the similarity of two sets [36]. Dice loss is a value ranging in [0, 1] which is defined as

$$\text{Dice Loss} = 1 - \text{Dice Coefficient} = 1 - \frac{2\left|\mathbf{I}_r \cap \mathbf{I}_p\right|}{|\mathbf{I}_r| + \left|\mathbf{I}_p\right|}. \quad (9)$$

The $\mathbf{I}_r$ is the real segmentation image of scatterers and $\mathbf{I}_p$ is the predicted segmentation image of scatterers, $\left|\mathbf{I}_r \cap \mathbf{I}_p\right|$ denotes the number of coincident pixels of $\mathbf{I}_r$ and $\mathbf{I}_p$, and $|\mathbf{I}_r|$ and $\left|\mathbf{I}_p\right|$ denotes the number of pixels of $\mathbf{I}_r$ and $\mathbf{I}_p$, respectively. There are two reasons for choosing the dice loss. One is that it is suitable for the situation where the number of positive samples ("scatterer" pixels) is greatly different from that of negative samples ("background" pixels) [36]. The other reason is that it directly uses evaluation indexes for training. The parameters of the U-Net will be adjusted for each training to minimize the dice loss. The optimization method used in this article is the Adam optimizer [37] with the hyperparameters $\beta_1 = 0.9$, $\beta_2 = 0.999$, $\epsilon = 0$ and the learning rate being equal to $1 \times 10^{-4}$.

## III. Numerical Results

In this section, we use three numerical examples to verify the proposed hybrid method. In the first example, it is assumed that an inhomogeneous scatterer is located in free space and we have to invert for the dielectric parameters on each pixel. The purpose of this case is to validate the feasibility and efficiency of the threefold hybrid method. In the second example, multiple isolated homogeneous scatterers are located in the DOI. We can merge dielectric parameters in all pixels of the same scatterer in the cost function since they share the same values in the inversion. In this case, the reconstruction ability of the hybrid method for scatterers with high contrasts

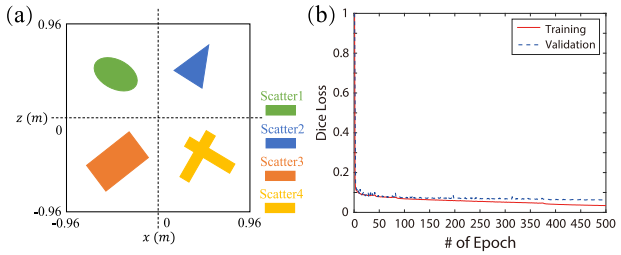


Fig. 3. (a) Training and validation models in case 1. (b) Convergence curves of training and validation in case 1.

is validated and the antinoise ability is also tested. In the third example, the generalization ability of the proposed hybrid method is tested. The shapes of the three scatterers are very different from those used in the training sets. All the measured scattered field data are simulated by the BCGS-FFT forward solver. In addition, in order to quantitatively evaluate the reconstruction performance of the proposed method, we use the data misfit and model misfit defined in (17) and (16) of [38]. The data misfit indicates how well the measured scattered fields match the predicted scattered fields in the iterations. The model misfit indicates how well the reconstructed model parameters match the true model parameters. All the numerical experiments are performed on a workstation with 20-cores Xeon E2650 v3 2.3 G CPU, 512 GB RAM. It approximately spends 14 h to generate 3500 training samples in the following two cases and the U-Net is trained on an NVIDIA Titan Xp GPU by using these 3500 samples. The architectures of the U-Nets in the two cases are the same but the training samples are different.

### A. EM Inversion Setups

The operating frequency is 300 MHz in both numerical examples. Totally, 72 transmitters and 72 receivers are uniformly placed on a circle with a radius of 10 m. We empirically choose this configuration for transmitters and receivers since numerical simulations show that continue to increase the transmitters and receivers almost have no aid for the FWI results. However, reducing transmitters and receivers has obvious negative effects on the inversion results. The inverse domain has the dimensions of 1.92 m $\times$ 1.92 m and is divided into 96 $\times$ 96 pixels with its center at the origin. The EM Inversion model is shown in Fig. 1.

### B. Csse 1: A Single Inhomogeneous Scatterer

As shown in Fig. 3(a), there are four basic shapes in the training set, including the ellipse, the triangle, the rectangle, and the cross. Only one shape appears in a training sample. Its sizes and locations are random but its total number of pixels is limited between 300 and 3000 to avoid too small or too big scatterers. Its relative permittivity is randomly set in the range of [2.0, 4.0], and the conductivity is assigned a random value between 10 and 30 mS/m. It should be pointed out that the scatterer in each training set is homogeneous. Therefore, we train the U-Net with homogeneous scatterers and generalize it to inhomogeneous scatterers. The input data for the U-Net are obtained by LSM. Using the above strategy, 3000 samples are randomly generated for training and 500 validation samples are generated for the adjustment of hyperparameters. After 500 epochs of training in a single Titan Xp GPU which costs about 3 hours, the training dice loss decreases to less than 0.04 and the validation dice loss becomes less than 0.07, as shown in Fig. 3(b). This means that after 500 epochs, the similarity between the segmented images predicted by U-Net and the real labels has exceeded 90%.

In the online prediction, we use four testing sets. Their ground truths are shown in the 1st and 2nd columns of Fig. 4. And the LSM imaging results are shown in the 3rd column. They are obtained by

$$G(\mathbf{r}_p) = -2\ln\left\|\hat{\mathbf{g}}(\theta, \mathbf{r}_p)\right\|_2 \tag{10}$$

in which $\hat{\mathbf{g}}$ is given in (4). Here, we calculate the reciprocal of $\|\hat{\mathbf{g}}\|_2^2$ and use the logarithm operation to get better visual effect. From the 3rd column of Fig. 4, it can be seen that LSM can recover the approximate shapes of scatterers. But the imaging effect is poor for the nonconvex envelopes and the sharp corners of scatterers, as shown in Fig. 4(h) and (m). For scatterers without nonconvex envelopes such as those in Test #4, the imaging result is better, as shown in Fig. 4(r). We then simply set a threshold to classify "scatterer" pixels and "background" pixels. The threshold is determined by

$$\text{threshold} = C \max_{\mathbf{r}_p} G(\mathbf{r}_p) \tag{11}$$

where $C$ is an empirical constant. We vary the value of $C$ until achieving the "best visual" reconstruction [8]. The classification results through the threshold are shown in the 4th of Fig. 4. And the classification results by U-Net are shown in the 5th column of Fig. 4. As can be seen, the classification results of U-Net are much better than those by the threshold. The reason is that the classification by the threshold is linear, while U-Net can extract nonlinear features from LSM results for classification.

After obtaining the classification results of LSM outputs, BIM is used for the FWI only in the "scatterer" pixels. We compare the inversion results by BIM implemented in the whole inversion domain, by BIM implemented in the "scatterer" region judged via the threshold classification, and by BIM implemented in the "scatterer" region judged via the U-Net classification. The results are shown in Fig. 5. As illustrated in the 1st and 4th columns, due to the ill-posedness of the inversion problem and the underdetermination of the discretized data equation, the model parameters obtained by BIM performed in the whole inversion domain are sometimes not accurate. For example, in Test #1 and Test #2, the reconstructed scatterer volumes are larger than the true volumes. As a result, the inverted dielectric parameter values are smaller than the real values. In Test #3, the shapes of the scatterer for the permittivity and conductivity reconstruction are not consistent. The results of BIM performed in the "scatterer" region determined by the threshold are shown in the 2nd and 5th columns of Fig. 5. Although the inversion domain is compressed and the unknowns in the discretized data equation are reduced, the inversion results are not good enough. The reason is that the shapes reconstructed by the LSM and

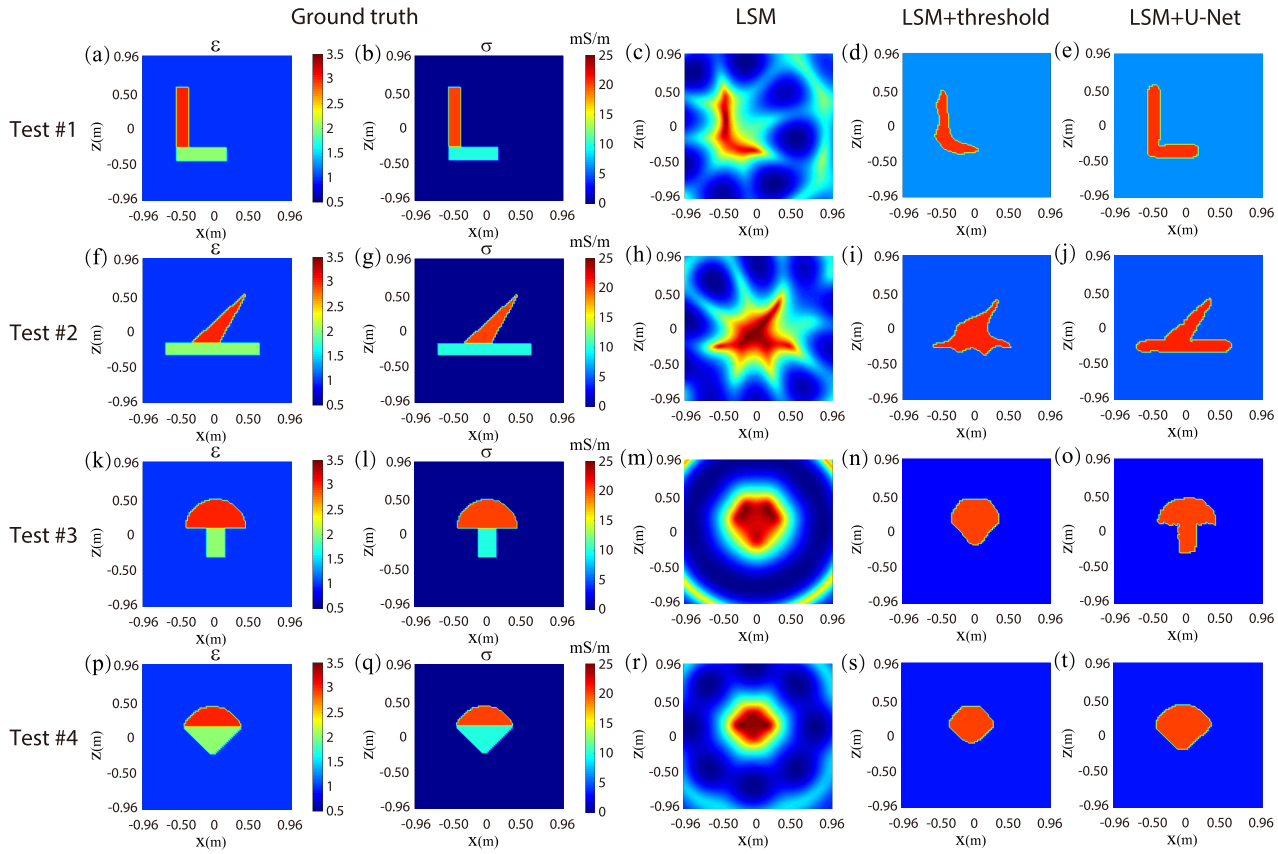


Fig. 4. Ground truths, LSM results, and the pixel classification results based on the threshold and U-Net in Test #1 - #4.

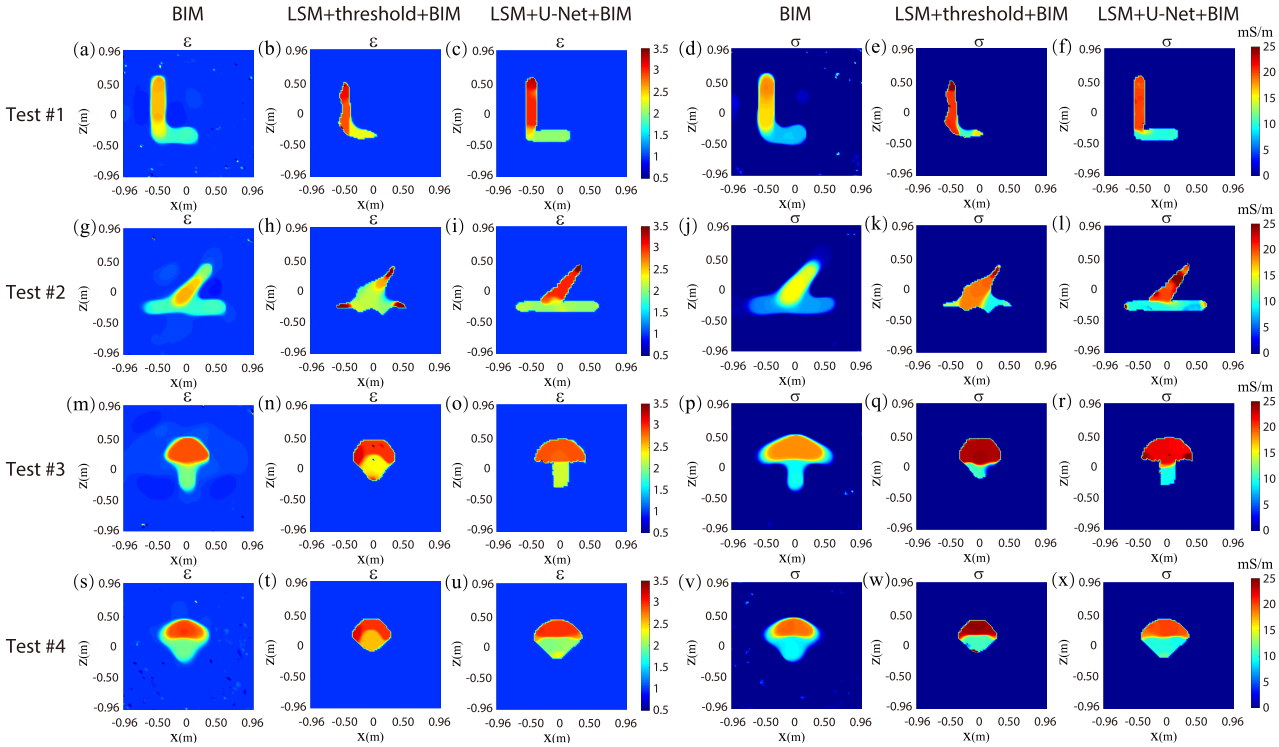


Fig. 5. Inversion results by BIM implemented in the whole inversion domain, by BIM implemented in the "scatterer" region judged via the threshold classification, and by BIM implemented in the "scatterer" region judged via the U-Net classification.

refined by the threshold are not precise enough. Consequently, the inverted permittivity and conductivity of the scatterers are not accurate although the computational cost of memory and time is saved. On the contrary, the inversion results based on the U-Net classification are better, regardless of the scatterer shapes or dielectric parameters, since the recovered shapes

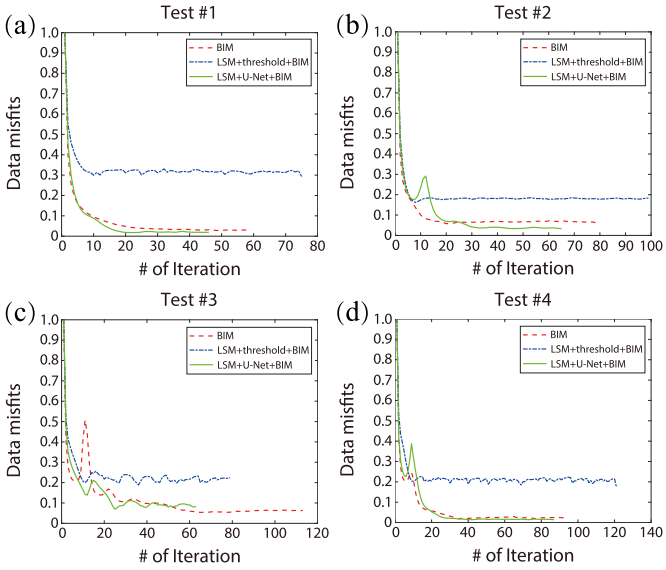


Fig. 6. Comparisons of convergence curves of BIM for the three methods in four tests.

TABLE I

MODEL MISFITS (%) FOR BIM, LSM+TH+BIM, AND LSM+U-NET+BIM

| Test \ Method | | BIM | LSM+TH+BIM | LSM+U-Net+BIM |
|---|---|---|---|---|
| Test #1 | $\varepsilon$ | 17.05 | 23.60 | 7.83 |
| | $\sigma$ | 62.43 | 73.11 | 25.53 |
| Test #2 | $\varepsilon$ | 16.69 | 24.64 | 13.71 |
| | $\sigma$ | 57.34 | 64.58 | 37.74 |
| Test #3 | $\varepsilon$ | 16.05 | 31.21 | 13.82 |
| | $\sigma$ | 49.31 | 58.05 | 36.92 |
| Test #4 | $\varepsilon$ | 10.07 | 21.58 | 6.92 |
| | $\sigma$ | 35.30 | 79.05 | 18.86 |

Remark: TH represents "threshold".

from the U-Net classification are closer to the true shapes of scatterers, as are shown in the 3rd and 6th columns of Fig. 5.

The data misfit variations in BIM iterations for different inversion domains are shown in Fig. 6. Because the true shapes of scatterers are quite different from the shapes recovered by LSM and the threshold, this method has the largest data misfits among the three methods. However, for BIM performed in the whole region, although the reconstructed model parameters are not accurate enough, the data misfits can achieve low values because the problem is underdetermined. Table I shows the model misfits of reconstructed permittivity and conductivity. We can see that the inversion based on the U-Net classification has the smallest model misfits for all cases. Another superiority of the proposed threefold hybrid method is that it has less time for single-step iteration due to the reduction of the inversion domain. For example, in Test #1, the mean single-step iteration time of BIM performed in the whole inversion domain is 623 s, while that based on U-Net classification results is only 132 s.

### *C. Case 2: Multiple Isolated Homogeneous Scatterers With High Contrasts*

As shown in Fig. 7(a), the basic shapes in the training set in this case are similar to those in case 1. However,

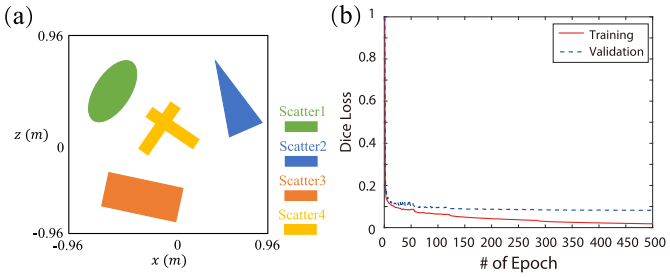


Fig. 7. (a) Training and validation models in case 2. (b) Convergence curves of training and validation in case 2.

multiple shapes are allowed to appear simultaneously in one training sample. These shapes can locate randomly in the inversion domain but are not allowed to overlap with each other. The sizes are also random but the total number of pixels taken by the scatterers is limited between 300 and 3000. Their relative permittivities are randomly set in the range of [5.0, 8.0], and conductivities are assigned random values between 50 and 80 mS/m. Compared with case 1 presented in Section III-B, the contrasts of scatterers with respect to the background air are much larger. There are also 3000 training samples and 500 validation samples and the training is carried out 500 epochs. When the training finishes, the training dice loss decreases to less than 0.02 and the validation dice loss becomes less than 0.09, as shown in Fig. 7(b). In this case, the similarity between the segmented images predicted by U-Net and the real labels also exceeds 90%.

We validate the ability of the proposed method to reconstruct multiple scatterers with high contrasts as well as its antinoise ability in three tests. The ground truths of these tests are shown in Fig. 8. From Test #5 to #7, the shapes of scatterers become more and more complex. The reconstruction performance of the proposed hybrid method under the noise-free, 20 dB noise, and 10 dB noise is compared. Here, the noise level is defined according to the signal-to-noise ratio (SNR) of power. In Fig. 9, the first, second, and third columns show the LSM imaging results when three levels of noise are added. Compared with those in case 1, the imaging results of multiple scatterers with high contrasts are much worse. This is not only due to the high contrasts but also the strong cross scattering among different scatterers. As shown in Fig. 9(g) and (m), the scatterer images from LSM connect together. In addition, it can be seen from the 2nd and 3rd columns that 20 dB noise has little influence on the imaging results. However, when the noise reaches 10 dB, they become obviously worse, especially in Test #7. Fortunately, the poor imaging results of LSM can be significantly improved by U-Net, which is shown in the 4th, 5th, and 6th columns of Fig. 9. We can see that the connections among multiple scatterers in the images disappear. Of course, the influence of cross scattering and noise cannot be completely eliminated by U-Net. The more scatterers and the larger noise are added, the worse is the scatterer images, as shown in Fig. 9(r).

Since each isolated scatterer is homogeneous, we can merge all the unknown dielectric parameters belonging to the same scatterer in the discretized data equation as long as

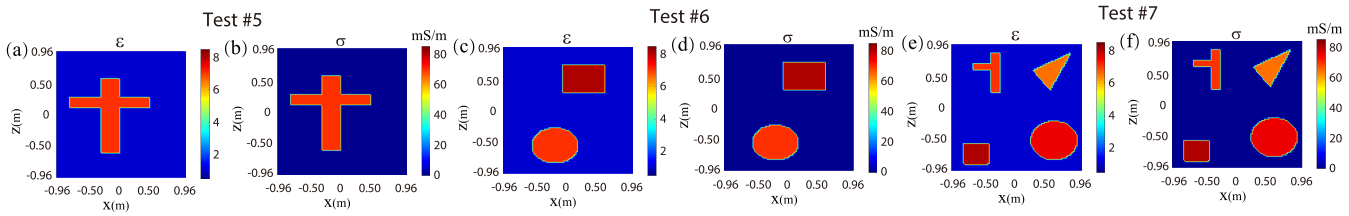


Fig. 8. Ground truths of three tests in case 2.

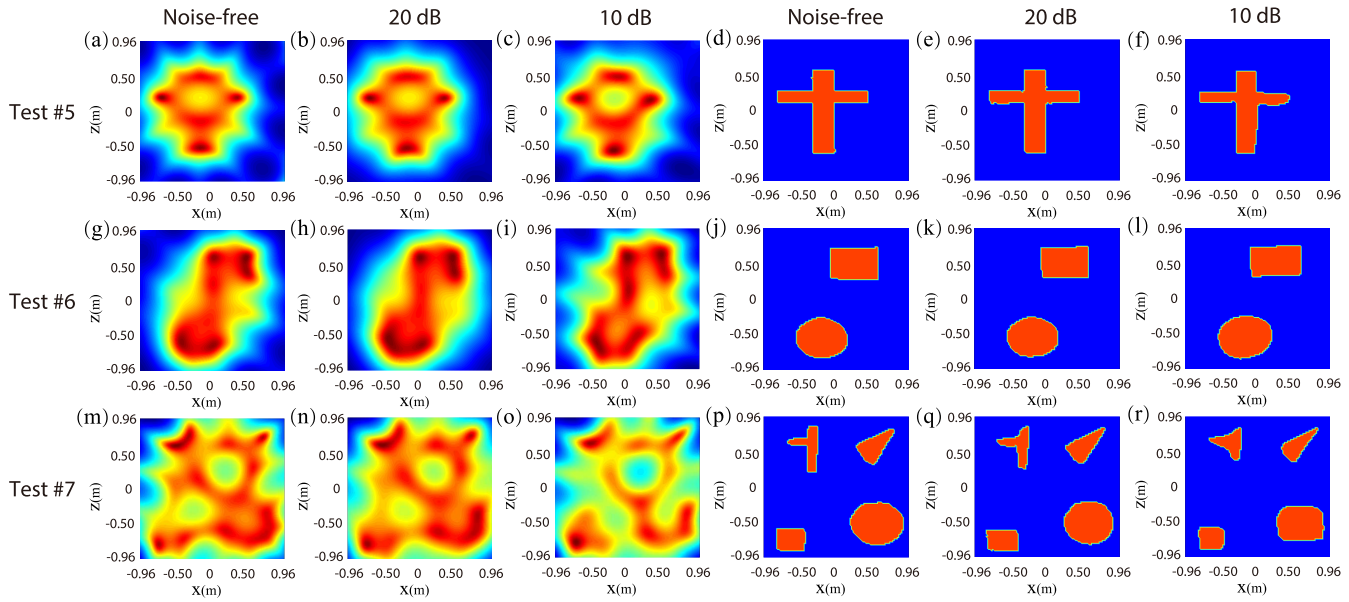


Fig. 9. LSM results and U-Net classification results under three different noise levels. Columns 1–3 show the LSM results. Columns 4–6 show the U-Net classification results.

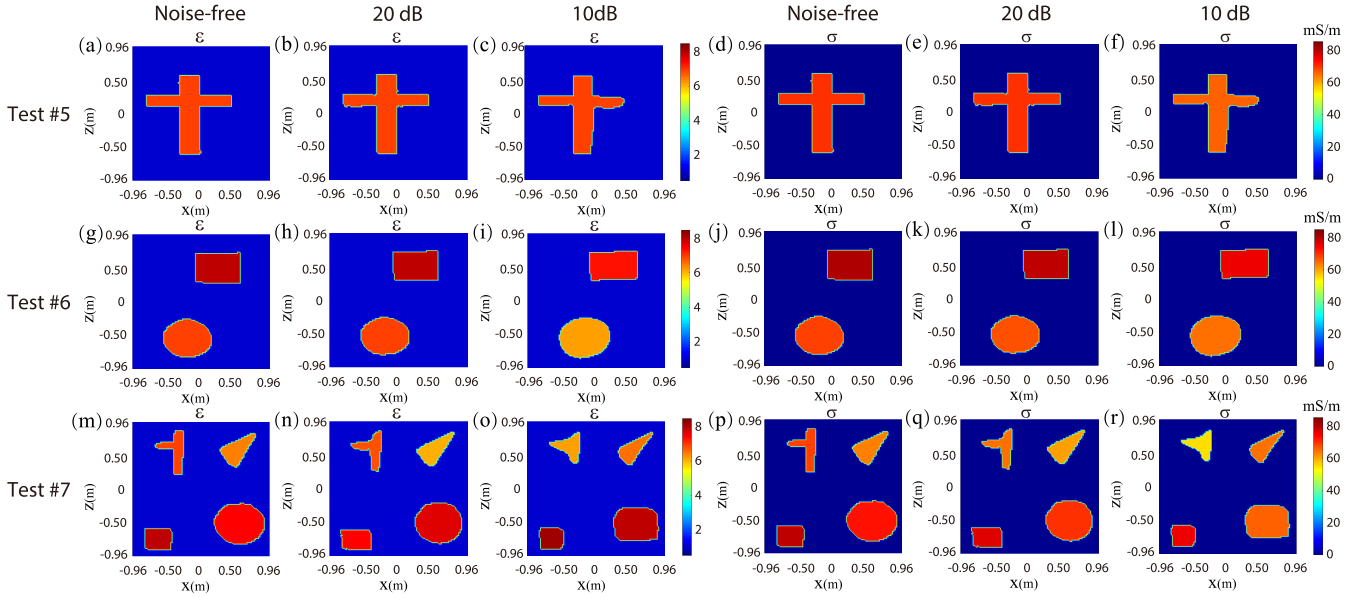


Fig. 10. FWI results by BIM implemented in the "scatterer" region judged via the U-Net classification under different noise levels. Columns 1–3 show the reconstructed permittivity. Columns 4–6 show the reconstructed conductivity.

the boundary of the isolated scatterer is located by U-Net. In this way, the BIM only needs to solve a very limited number of unknowns. The dielectric parameters reconstructed by BIM based on the shapes in Fig. 9 are shown in Fig. 10. We can see that the proposed hybrid method is capable of reconstructing multiple scatterers with large contrasts even when the measured scattered field data are contaminated by noise. When the noise level is too high, e.g., 10 dB, the shapes reconstructed by U-Net are severely distorted, which leads to the deviation of the permittivity and conductivity obtained

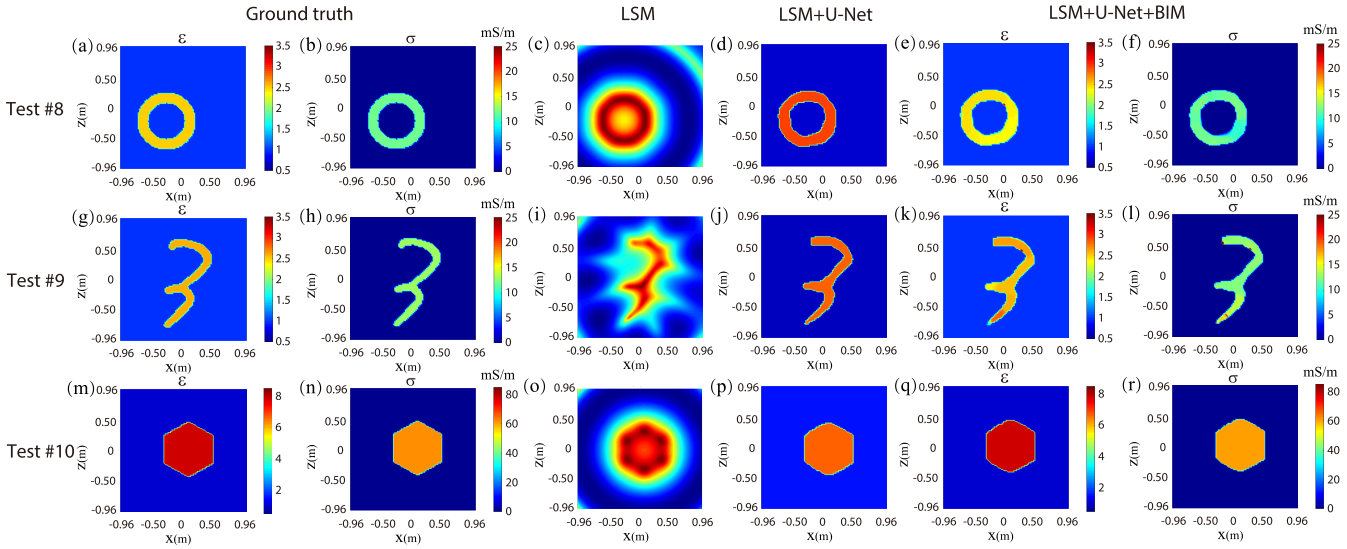


Fig. 11. Ground truths, LSM results, U-Net results, and FWI results by BIM implemented in the "scatterer" region judged via the U-Net classification.

TABLE II
MODEL MISFITS (%) OF INVERTED PARAMETERS WHEN THE SCATTERED FIELD DATA ARE CONTAMINATED BY NOISE WITH DIFFERENT SNRS

| Test \ noise-level | | noise-free | 20 dB | 10 dB |
|---|---|---|---|---|
| Test #5 | $\varepsilon$ | 4.10 | 9.72 | 31.71 |
| | $\sigma$ | 5.11 | 12.13 | 39.56 |
| Test #6 | $\varepsilon$ | 12.12 | 21.03 | 31.09 |
| | $\sigma$ | 14.77 | 25.46 | 37.62 |
| Test #7 | $\varepsilon$ | 20.68 | 31.05 | 40.53 |
| | $\sigma$ | 24.94 | 37.46 | 48.91 |

by BIM, as shown in Fig. 10(r). The model misfits of all three tests with different noise levels are listed in Table II. One obvious observation is that the misfit increases with the increase of scatterer number and noise level. Although the U-Net can improve the LSM imaging results, the shape distortion cannot be absolutely avoided.

### D. Case 3: Generalization Ability Tests

In order to test the generalization ability of the proposed hybrid method, we apply it to three scatterers whose shapes are far from those in the training sets. As shown in Fig. 11, the relative permittivity and conductivity of the hollow ring are 2.5 and 12 mS/m, respectively. Its LSM image resembles a solid disk. However, the reconstructed shape by the same U-Net which has been used in Case 1 is close to the true hollow shape. Based on this, the reconstructed dielectric parameters are also close to the true values. Similarly, we apply the same U-Net to the character "3" in the MNIST database [39]. The relative permittivity and conductivity of the character are 2.6 and 13 mS/m, respectively. As shown in Fig. 11(g)–(l), both the reconstructed shape and dielectric parameter values are close to the ground truths. We also test the generalization ability of the U-Net used in Case 2 through a hexagon with high contrast, as shown in Fig. 11(m)–(r). We can see that the parameters are also well reconstructed although the LSM image looks like a disk.

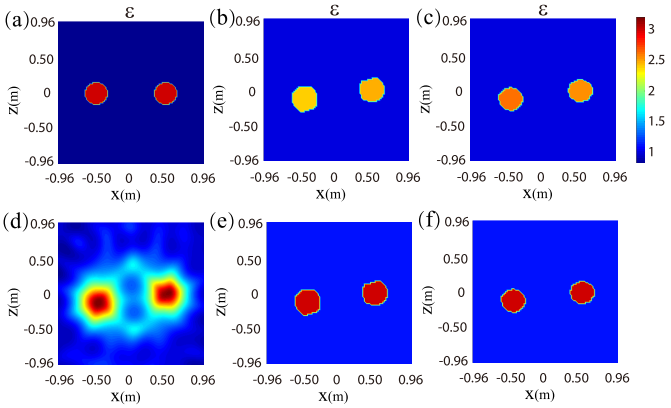


Fig. 12. Imaging and FWI results of the experimental data measured at Institute Fresnel. (a) Ground truth of $\varepsilon$. (b) Retrieved $\varepsilon$ by LSM+threshold+BIM. (c) Retrieved $\varepsilon$ by LSM+U-Net+BIM. (d) Result of LSM. (e) Classification result using the threshold. (f) Classification result using U-Net.

## IV. TESTS WITH EXPERIMENTAL DATA

The experimental data measured at Institute Fresnel [40] are used to further evaluate the proposed method. A "twodielTM" profile is adopted in the test. In the measurement environment, both the transmitter and receiver arrays are placed on a circle with the radius of 1.67 m surrounding the "twodielTM" profile. The operating frequency is 5 GHz. Totally 36 transmitters are used and the field data are recorded by 49 receivers. The experimental data are calibrated by multiplying them with a single complex-valued coefficient which is derived from the ratio of the measured incident field and the simulated one at the receiver located at the opposite position of the source [18], [41]. The U-Net used in this case is the same as that in case 2. The ground truth is shown in Fig. 12(a), and the result of LSM is shown in Fig. 12(d). The results

of threshold classification and U-Net classification are shown in Fig. 12(e) and (f), respectively. Parts (b) and (c) of Fig. 12 are the FWI results of relative permittivity by BIM based on threshold classification and U-Net classification, respectively. The model misfits of the permittivity based on threshold classification and U-Net classification are 15.02% and 13.65%, respectively. Meanwhile, the final data misfits when BIM iteration terminates are 36.63% and 36.00%, respectively. Because the images obtained through the threshold classification and U-Net classification have no big difference, the permittivity values reconstructed by BIM are also close, as shown in Fig. 12(b) and (c). The results from the experimental data further validate the effectiveness of the proposed hybrid method for dealing with the laboratory-measured data.

## V. Conclusion and Future Work

In this article, a threefold hybrid EM inversion method is proposed. It combines and utilizes the respective advantage of LSM, U-Net, and BIM. The LSM acquires the approximate shapes and locations of the scatterers at a low computational cost. The trained U-net further refines the shapes almost in a real-time fashion. And finally, BIM is implemented to retrieve the dielectric parameters of the scatterers. Because the inversion domain is compressed and it becomes close to the true shapes of scatterers, the number of unknowns solved by BIM decreases. As a result, the ill-posedness is mitigated, the inversion accuracy is enhanced, and the computational cost is lowered.

Two numerical examples are used to validate the performance of the proposed method. The final reconstructed results show the feasibility of the threefold hybrid method. The comparisons between the hybrid and the traditional methods show that the proposed method outperforms the pure BIM for inversion accuracy. In case 2, we show the performance of this method for dealing with noisy data and scatterers with high contrasts. It is found that the hybrid method can still obtain reliable results for multiple scatterers with high contrasts even when the measured scattered field data are contaminated by 10 dB noise. In case 3, laboratory-measured data are used to validate the feasibility of the method.

In this work, the hybrid method is applied to the reconstruction of 2-D scatterers placed in a homogeneous background medium. The future work will be focused on three aspects. (1) Combine the 3-D LSM [8], 3-D U-Net [27], and the 3-D FWI [42] to reconstruct 3-D anisotropic scatterers. This can highlight the advantages of the proposed method in reducing time cost and memory consumption more obviously. (2) Apply the hybrid method to the reconstruction of scatterers buried in a layered medium. In this situation, the apertures of the transmitter and receiver arrays are restricted in a certain range, which is more practical in many real-world applications, e.g., the GPR geophysical exploration [7]. (3) Compare the training cost of different types of ANNs used in FWI. In this work, both the input and output of the CNN are pure images. The physics-assisted learning presented in [18], [26], and [27] adopt similar approaches in which the input and output of CNNs are permittivity values in all the pixels. By contrast, the direct learning schemes in [18]–[20] directly convert the measured scattered fields into the dielectric parameters. The CNNs in all these applications usually have different structures or loss functions. It is not easy to compare their training cost. However, it is intuitive that the direct learning scheme has a high training cost since the ANN must learn the underlying wave physics of EM scattering. This has been demonstrated in Fig. 4 of [18] since the direct learning scheme has the worst inversion results compared with other methods based on the same trained ANN. Of course, the strict proof of the training cost of different ANNs in FWI will be left as future work.

## References


[1] M. S. Zhdanov, *Geophysical Inverse Theory and Regularization Problems*. Amsterdam, The Netherlands: Elsevier, 2002.

[2] K. D. Paulsen, S. P. Poplack, D. Li, M. W. Fanning, and P. M. Meaney, "A clinical prototype for active microwave imaging of the breast," *IEEE Trans. Microw. Theory Techn.*, vol. 48, no. 11, pp. 1841–1853, Nov. 2000.

[3] M. Younis, J. Maurer, J. Fortuny-Guasch, R. Schneider, W. Wiesbeck, and A. J. Gasiewski, "Interference from 24-GHz automotive radars to passive microwave earth remote sensing satellites," *IEEE Trans. Geosci. Remote Sens.*, vol. 42, no. 7, pp. 1387–1398, Jul. 2004.

[4] F. Garcia-Rial, D. Montesano, I. Gómez, C. Callejero, F. Bazus, and J. Grajal, "Combining commercially available active and passive sensors into a millimeter-wave imager for concealed weapon detection," *IEEE Trans. Microw. Theory Techn.*, vol. 67, no. 3, pp. 1167–1183, Mar. 2019.

[5] B. Yektakhah and K. Sarabandi, "All-directions through-the-wall imaging using a small number of moving omnidirectional bi-static FMCW transceivers," *IEEE Trans. Geosci. Remote Sens.*, vol. 57, no. 5, pp. 2618–2627, May 2019.

[6] X. Zhuge, A. G. Yarovoy, T. Savelyev, and L. Ligthart, "Modified kirchhoff migration for UWB MIMO array-based radar imaging," *IEEE Trans. Geosci. Remote Sens.*, vol. 48, no. 6, pp. 2692–2703, Jun. 2010.

[7] H. Liu, Z. Long, F. Han, G. Fang, and Q. H. Liu, "Frequency-domain reverse-time migration of ground penetrating radar based on layered medium Green's functions," *IEEE J. Sel. Topics Appl. Earth Observ. Remote Sens.*, vol. 11, no. 8, pp. 2957–2965, Aug. 2018.

[8] D. Colton, H. Haddar, and M. Piana, "The linear sampling method in inverse electromagnetic scattering theory," *Inverse Problems*, vol. 19, no. 6, pp. S105–S137, Nov. 2003.

[9] I. Catapano, L. Crocco, and T. Isernia, "On simple methods for shape reconstruction of unknown scatterers," *IEEE Trans. Antennas Propag.*, vol. 55, no. 5, pp. 1431–1436, May 2007.

[10] B. Engquist, *Encyclopedia of Applied and Computational Mathematics*. Berlin, Germany: Springer, 2016. [Online]. Available: https://link.springer.com/referencework/10.1007/978-3-540-70529-1

[11] W. Hu, A. Abubakar, and T. M. Habashy, "Integrated imaging and inversion of multi-physics data for exploration geopysics applications," in *Proc. 2nd IEEE Int. Workshop Comput. Adv. Multi-Sensor Adapt. Process.*, Dec. 2007, pp. 169–172.

[12] G. Bozza, C. Estatico, M. Pastorino, and A. Randazzo, "An inexact Newton method for microwave reconstruction of strong scatterers," *IEEE Antennas Wireless Propag. Lett.*, vol. 5, no. 1, pp. 61–64, Dec. 2006.

[13] Y. M. Wang and W. C. Chew, "An iterative solution of the two-dimensional electromagnetic inverse scattering problem," *Int. J. Imag. Syst. Technol.*, vol. 1, no. 1, pp. 100–108, 1989.

[14] F. Li, Q. H. Liu, and L.-P. Song, "Three-dimensional reconstruction of objects buried in layered media using Born and distorted Born iterative methods," *IEEE Geosci. Remote Sens. Lett.*, vol. 1, no. 2, pp. 107–111, Apr. 2004.

[15] P. M. V. D. Berg and R. E. Kleinman, "A contrast source inversion method," *Inverse Problems*, vol. 13, no. 6, pp. 1607–1620, Dec. 1997.

[16] X. Chen, "Subspace-based optimization method for solving inverse-scattering problems," *IEEE Trans. Geosci. Remote Sens.*, vol. 48, no. 1, pp. 42–49, Jan. 2010.

[17] X. Chen, Z. Wei, M. Li, and P. Rocca, "A review of deep learning approaches for inverse scattering problems," *Prog. Electromagn. Res.*, vol. 167, pp. 67–81, 2020.

[18] Z. Wei and X. Chen, "Deep-learning schemes for full-wave nonlinear inverse scattering problems," *IEEE Trans. Geosci. Remote Sens.*, vol. 57, no. 4, pp. 1849–1860, Apr. 2019.

[19] H. M. Yao, W. E. I. Sha, and L. Jiang, "Two-step enhanced deep learning approach for electromagnetic inverse scattering problems," *IEEE Antennas Wireless Propag. Lett.*, vol. 18, no. 11, pp. 2254–2258, Nov. 2019.
[20] L.-Y. Xiao, J. Li, F. Han, W. Shao, and Q. H. Liu, "Dual-module NMM-IEM machine learning for fast electromagnetic inversion of inhomogeneous scatterers with high contrasts and large electrical dimensions," *IEEE Trans. Antennas Propag.*, vol. 68, no. 8, pp. 6245–6255, Aug. 2020.
[21] R. Guo, X. Song, M. Li, F. Yang, S. Xu, and A. Abubakar, "Supervised descent learning technique for 2-D microwave imaging," *IEEE Trans. Antennas Propag.*, vol. 67, no. 5, pp. 3550–3554, May 2019.
[22] S. Lu, B. Liang, J. Wang, F. Han, and Q. H. Liu, "1-D inversion of GREATEM data by supervised descent learning," *IEEE Geosci. Remote Sens. Lett.*, early access, Feb. 1, 2021, doi: 10.1109/LGRS.2021.3053247.
[23] G. Chen, P. Shah, J. Stang, and M. Moghaddam, "Learning-assisted multimodality dielectric imaging," *IEEE Trans. Antennas Propag.*, vol. 68, no. 3, pp. 2356–2369, Mar. 2020.
[24] P. Mojabi, V. Khoshdel, and J. Lovetri, "Tissue-type classification with uncertainty quantification of microwave and ultrasound breast imaging: A deep learning approach," *IEEE Access*, vol. 8, pp. 182092–182104, 2020.
[25] Y. Sanghvi, Y. Kalepu, and U. K. Khankhoje, "Embedding deep learning in inverse scattering problems," *IEEE Trans. Comput. Imag.*, vol. 6, pp. 46–56, 2020.
[26] L. Li, L. G. Wang, F. L. Teixeira, C. Liu, A. Nehorai, and T. J. Cui, "DeepNIS: Deep neural network for nonlinear electromagnetic inverse scattering," *IEEE Trans. Antennas Propag.*, vol. 67, no. 3, pp. 1819–1828, Mar. 2019.
[27] J. Xiao, J. Li, Y. Chen, F. Han, and Q. H. Liu, "Fast electromagnetic inversion of inhomogeneous scatterers embedded in layered media by Born approximation and 3-D U-Net," *IEEE Geosci. Remote Sens. Lett.*, vol. 17, no. 10, pp. 1677–1681, Oct. 2020.
[28] Z. Wei and X. Chen, "Physics-inspired convolutional neural network for solving full-wave inverse scattering problems," *IEEE Trans. Antennas Propag.*, vol. 67, no. 9, pp. 6138–6148, Sep. 2019.
[29] Y. Chen, J. Li, J. Zhuo, F. Han, and Q. H. Liu, "Fast multiparametric electromagnetic full-wave inversion via solving contracting scattering data equations optimized by the 3-D MRF model," *IEEE Trans. Microw. Theory Techn.*, vol. 68, no. 11, pp. 4515–4527, Nov. 2020.
[30] A. Massa, D. Marcantonio, X. Chen, M. Li, and M. Salucci, "DNNs as applied to electromagnetics, antennas, and Propagation—A review," *IEEE Antennas Wireless Propag. Lett.*, vol. 18, no. 11, pp. 2225–2229, Nov. 2019.
[31] X. Tang, J. Li, L. Wang, F. Han, H. Liu, and Q. H. Liu, "Hybrid reconstruction of subsurface 3-D objects using FRTM and VBIM enhanced by Monte Carlo method," *IEEE Geosci. Remote Sens. Lett.*, vol. 18, no. 2, pp. 213–217, Feb. 2021.
[32] E. A. Marengo and R. W. Ziolkowski, "Nonradiating and minimum energy sources and their fields: Generalized source inversion theory and applications," *IEEE Trans. Antennas Propag.*, vol. 48, no. 10, pp. 1553–1562, Oct. 2000.
[33] T. Lan, N. Liu, Y. Liu, F. Han, and Q. H. Liu, "2-D electromagnetic scattering and inverse scattering from magnetodielectric objects based on integral equation method," *IEEE Trans. Antennas Propag.*, vol. 67, no. 2, pp. 1346–1351, Feb. 2019.
[34] B. Wohlberg and P. Rodriguez, "An iteratively reweighted norm algorithm for minimization of total variation functionals," *IEEE Signal Process. Lett.*, vol. 14, no. 12, pp. 948–951, Dec. 2007.
[35] O. Ronneberger, P. Fischer, and T. Brox, "U-Net: Convolutional networks for biomedical image segmentation," in *Proc. Int. Conf. Med. Image Comput. Comput.-Assist. Intervent.*, 2015, pp. 234–241.
[36] F. Milletari, N. Navab, and S.-A. Ahmadi, "V-Net: Fully convolutional neural networks for volumetric medical image segmentation," in *Proc. 4th Int. Conf. 3D Vis. (3DV)*, Oct. 2016, pp. 565–571.
[37] D. P. Kingma and J. Ba, "Adam: A method for stochastic optimization," 2014, *arXiv:1412.6980*. [Online]. Available: http://arxiv.org/abs/1412.6980
[38] T. Lan, N. Liu, F. Han, and Q. H. Liu, "Joint petrophysical and structural inversion of electromagnetic and seismic data based on volume integral equation method," *IEEE Trans. Geosci. Remote Sens.*, vol. 57, no. 4, pp. 2075–2086, Apr. 2019.
[39] Y. Lecun, L. Bottou, Y. Bengio, and P. Haffner, "Gradient-based learning applied to document recognition," *Proc. IEEE*, vol. 86, no. 11, pp. 2278–2324, Nov. 1998.
[40] K. Belkebir and M. Saillard, "Testing inversion algorithms against experimental data," *Inverse Problems*, vol. 17, no. 6, p. 1565, 2001.
[41] J.-M. Geffrin, P. Sabouroux, and C. Eyraud, "Free space experimental scattering database continuation: Experimental set-up and measurement precision," *Inverse Problems*, vol. 21, no. 6, pp. S117–S130, Dec. 2005.
[42] J. Li, J. Zhuo, Z. Guan, F. Han, and Q. H. Liu, "3-D electromagnetic scattering and inverse scattering by magnetodielectric objects with arbitrary anisotropy in layered uniaxial media," *IEEE Trans. Antennas Propag.*, vol. 68, no. 2, pp. 1009–1022, Feb. 2020.

**Yanjin Chen** received the B.S. degree in mechanical and electronic engineering from the Hainan University of China, Haikou, China, in 2017. He is currently pursuing the master's degree with Xiamen University, Xiamen, China.

His current research interest is applying the machine learning techniques to electromagnetic inverse scattering problems.

**Li-Ye Xiao** (Member, IEEE) received the B.S. and Ph.D. degrees in electronic information science and technology from the University of Electronic Science and Technology of China (UESTC), Chengdu, China, in 2015 and 2019, respectively.

In 2018, he was a Visiting Scholar with the Department of Electrical and Computer Engineering, Duke University, Durham, NC, USA. He is currently with the Institute of Electromagnetics and Acoustics, Xiamen University, Xiamen, China, as a Post-Doctoral Researcher. His current research interest is computational electromagnetics.

**Jianliang Zhuo** received the B.S. degree in communication engineering and business administration and the M.S. degree in communication and information system from the University of Electronic Science and Technology of China, Chengdu, China, in 2007 and 2011, respectively, and the Ph.D. degree in physical electronics from Xiamen University, Xiamen, China, in 2018.

His research interests include fast forward solvers in electromagnetics and inverse scattering methods for microelectronics and RF systems.

**Feng Han** (Senior Member, IEEE) received the B.S. degree in electronic science from Beijing Normal University, Beijing, China, in 2003, the M.S. degree in geophysics from Peking University, Beijing, in 2006, and the Ph.D. degree in electrical engineering from Duke University, Durham, NC, USA, in 2011.

Since July 2015, he has been with Xiamen University, Xiamen, China, where he is currently an Associate Professor with the Institute of Electromagnetics and Acoustics. He has published over 40 articles in refereed journals. His research interests include electromagnetic scattering and inverse scattering in complex media, fast full-wave electromagnetic inversion based on machine learning, geophysical electromagnetic exploration and inversion, etc.

**Qing Huo Liu**, photograph and biography not available at the time of publication.